Letter

Information limit of 15 picometers achieved with bright-field ptychography

Haozhi Sha, Jizhe Cui, Wenfeng Yang, and Rong Yu*

School of Materials Science and Engineering, Tsinghua University, Beijing 100084, China;
MOE Key Laboratory of Advanced Materials, Tsinghua University, Beijing 100084, China;
and State Key Laboratory of New Ceramics and Fine Processing, Tsinghua University, Beijing 100084, China

(Received 20 December 2023; revised 19 May 2024; accepted 5 August 2024; published 26 August 2024)

It is generally assumed that a high spatial resolution of a microscope requires a large numerical aperture of the imaging lens or detector. In this study, the information limit of 15 pm is achieved in transmission electron microscopy using only the bright-field disk (small numerical aperture) via multislice ptychography. The results indicate that high-frequency information has been encoded in the bright-field disk due to the multiple scattering of electrons in the objects, making it possible to break the diffraction limit of imaging via bright-field ptychography.

DOI: 10.1103/PhysRevB.110.L060104

According to Abbe's theory of imaging, the space resolution of a microscope is limited by the diffraction effect of imaging waves [1–5]. The resolution limit can be generally written as $k\lambda$ /NA, where λ is the wavelength, NA stands for numerical aperture, which is $n\sin\alpha$ with n being the refraction index and α the semiangle of the objective lens aperture. The factor k varies with resolution criteria [2–5], being 0.61 for Rayleigh resolution, 0.5 for Abbe resolution, and 0.47 for Sparrow resolution, for example. In conventional electron microcopy, Scherzer adopts 0.8 for coherent imaging and 0.6 for incoherent imaging [5]. In scanning transmission electron microscopy (STEM), α is the convergence semiangle of the probe. Loosely speaking, k is about 1 for coherent modes like bright-field (BF) imaging, and about 0.5 for incoherent modes like high-angle annular dark-field (HAADF) imaging [6–8].

Electron ptychography is a diffractive imaging method that utilizes scattered electrons inside the collection angle β of the pixelated detector to retrieve the object information. Consequently, the largest scattering angle or effective aperture is now $\alpha + \beta$, and the diffraction limit of ptychography can be described as $k\lambda/\sin(\alpha + \beta)$. The electrons scattered to the largest angle carry information of the highest spatial frequency that the detector collects. In this way, high-angle scattering has been utilized to improve the resolution of ptychography [9–16]. The information limit reaches 39 pm with a large collection angle $\beta = 3\alpha$, which corresponds to $0.8\lambda/\sin(\alpha + \beta)$ [10].

It has been demonstrated that bringing a high-angle scattering wave outside the aperture back to the low frequency region can help to break the diffraction limit of imaging. For example, McCutchen noted that, by putting a stop right against the illuminated object, the low-frequency region of an image will contain contributions from high frequency information in the object due to the convolution process [17]. In optical microscopy, multiple scattering of light by disordered media can be utilized to overcome the diffraction limit [18,19]. It is also worth noting that resolution can be enhanced by allowing the iterative ptychography algorithm to recover the diffraction intensity in the frequency region beyond the collection angle of detectors [15,20,21].

Due to the strong interactions between incident electrons and objects, multiple scattering is common in electron microscopy. It usually leads to undesirable effects in diffraction, imaging, and spectroscopy. It is often necessary to develop techniques to mitigate multiple scattering effects. For example, dynamical electron diffraction prevents direct Fourier analysis in crystallography and precession electron diffraction is developed to reduce dynamic diffraction [22,23].

In this work, we show that multiple scattering of electrons can be used in multislice electron ptychography [12,24,25] to extend the information limit in the phase images without the aid of any additional medium or high-angle scattering. The information limit reaches 15 pm, corresponding to $0.44\lambda/\sin(\alpha + \beta)$.

First, we use simulation to demonstrate the effect of multiple scattering in ptychography. Four-dimensional (4D) datasets are simulated with the multislice method [26,27] for two thickness values, 0.8 and 20 nm, respectively. A perovskite oxide $DyScO_3$ in the [001] zone axis is used as the object. An electron beam of 300 kV and 25-mrad convergence semiangle is used to generate series of simulation datasets, which are divided into low-angle and high-angle groups, with the maximum collection semiangle of 27 mrad ($\beta \approx \alpha$) and 54 mrad ($\beta \approx 2\alpha$), respectively. The diffraction patterns in all the datasets have 120 × 120 pixels. Other simulation parameters are listed in Table S1 of the Supplemental Material [28]. Diffraction patterns in both the low-angle and high-angle groups are padded to 120 mrad with zero, resulting in a real space pixel size of 8.2 pm. In order to study only the effects of multiple scattering, the results in Fig. 1 exclude the effects of thermal diffuse scattering and noise. The influence of thermal diffuse scattering (TDS) is demonstrated in Fig. S1 [28] and Fig. 3(b),

*Contact author: ryu@tsinghua.edu.cn

 ©2024 American Physical Society

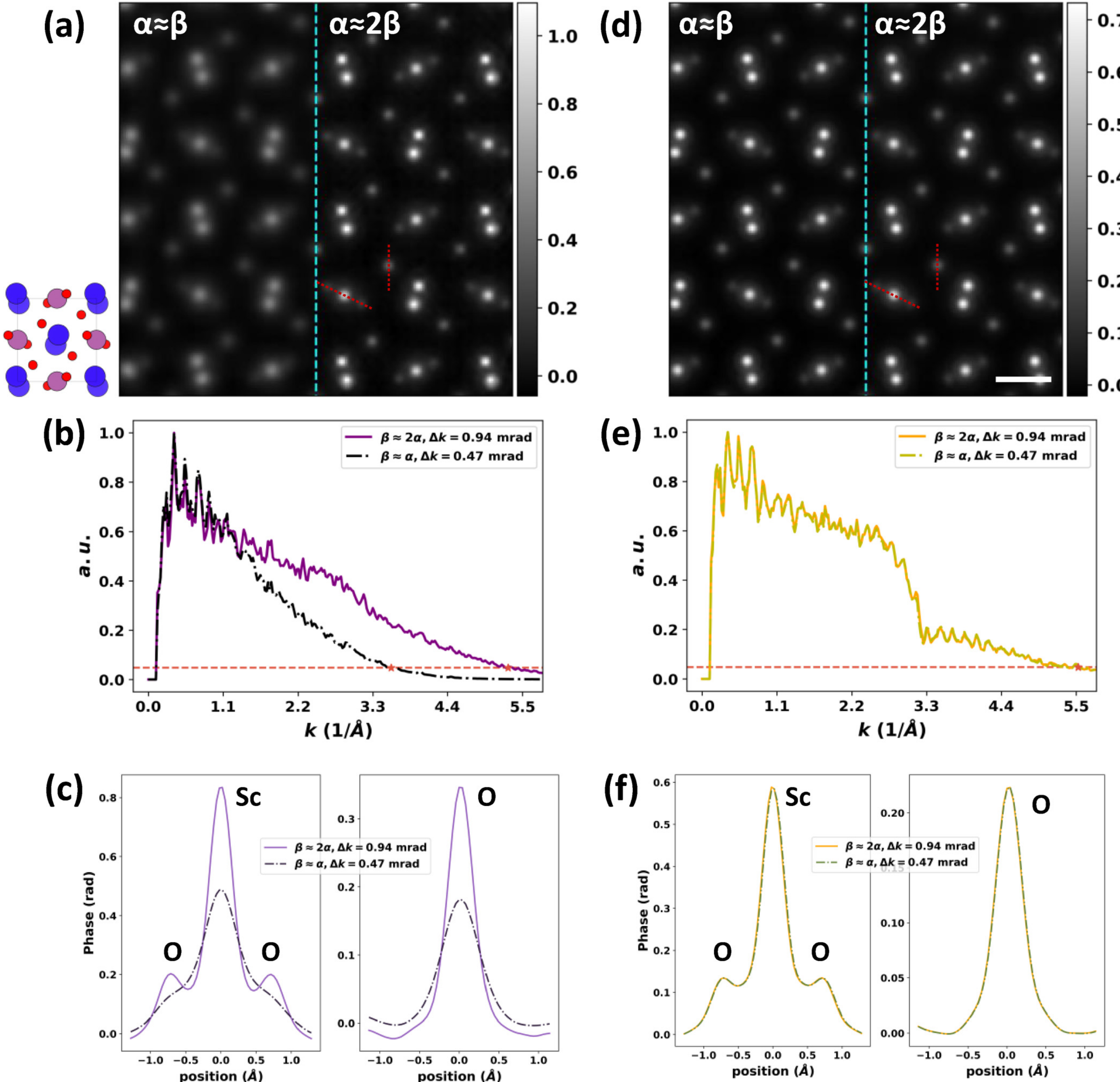

FIG. 1. Resolution improvement by using multiple scattering. Sample thickness of (a)–(c) is 0.8 nm, (d)–(f) 20 nm. (a), (d) Comparison of recovered mean phases based on datasets with different collection semiangle. Each phase image is averaged over all the slices. Collection angles are labeled on the top of each image. Slice thickness is chosen as 0.5 nm during multislice ptychographic reconstruction. The blue, purple, and red circles stand for Dy, Sc, and O atoms, respectively. Scale bar, 2 Å. (b), (e) Azimuthal average of the power spectrums corresponding to the phase images shown in (a) and (d). Information limits are marked with red stars. (c), (f) Phase profiles across the red dashed lines marked in (a) and (d).

which lead to the same conclusion as Fig. 1. Instead of allowing the iterative algorithm to fill in the extended region in diffraction pattern [15,20,21], we use the conventional Fourier constraint which forces the zero-padded region to zero during optimization.

Figure 1(a) displays the ptychographic phase images recovered from the simulation datasets of a 0.8-nm-thick sample. Figure 1(b) shows the radial profile of the corresponding power spectrum, with the information limits (d_{info}) labeled with red stars. Phase profiles across the atomic columns of O-Sc-O and isolated O are displayed in Fig. 1(c). It is evident that a large collection angle increases the information limit, which aligns with the observation in Ref. [10]. For very thin samples, most incident electrons are scattered at most once before reaching the detector. The kinematic approximation is applicable and the maximum scattering angle $\theta_{\max}$ of electrons collected by the detector increases with the collection semiangle β. As electrons scattered to high angles carry high frequency information, the information limit in the recovered phase images is limited by the collection

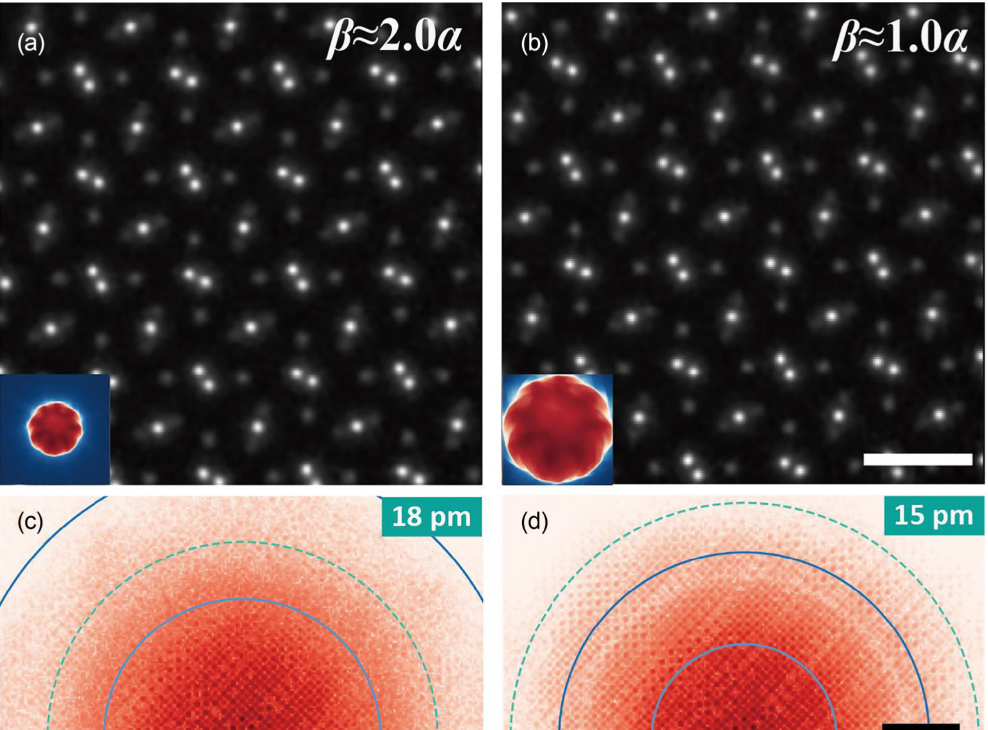

FIG. 2. Experimental results using different collection semiangles. (a), (b) Reconstructed $DyScO_3$ phase images averaged over slices free of the influence of surface damage. Slice thickness is 3 Å. Scale bar, 6 Å. Insets show PACBEDs. Sampling interval in reciprocal space is 0.042 and 0.021 $Å^{-1}$, respectively. (c), (d) Corresponding power spectrums of phases shown in (a) and (b). Information limits are marked with cyan dashed lines and labeled on the top left. Diffraction limits corresponding to $\lambda/(\alpha + \beta)$ and $0.5\lambda/(\alpha + \beta)$ are marked with light and dark blue solid lines, respectively. Scale bar, 2 $Å^{-1}$.

semiangle under the noise-free condition, as demonstrated in Figs. 1(a)–1(c).

Figure 1(d) shows the ptychographic phase images recovered from the simulation datasets of a 20-nm-thick sample. It is noticed that the phase image for the small collection angle is nearly the same as that for the large collection angle. As shown in Fig. 1(e), the information limit is the same for the small and large collection angles. The broadening widths of atomic columns become nearly identical for the two collection angles, as shown in Fig. 1(f), indicating that the BF disk contains sufficient high-frequency information that can be retrieved by multislice ptychography. Fourier ring correlation is also used to show the resolution enhancement in a thick sample (Fig. S2 [28]). When the thickness of samples increases, multiple scattering becomes prevalent, giving rise to rich features in the intensity of the BF disk. These features can be used to enhance the resolution through reconstruction algorithms that incorporate the multiple scattering processes. The additional information comes from two types of electrons: those absent in the BF disk due to the scattering into diffraction disks and those present in the BF disk carrying high-frequency information ($>2\alpha$). To comprehend the presence of the BF electrons with high-frequency information, it is essential to recognize that the maximum scattering angle that an electron may experience in multiple scattering is not limited by the collection angle. Electrons scattered to high angles can be scattered back and enter a low-angle aperture. Therefore, electrons that hit the low-angle area in a detector may also carry high-frequency information. We also combine Fisher information and scattering theory to discuss the possibility of using multiple scattering to enhance the resolution in the Supplemental Material [28].

Furthermore, we demonstrate in experiment that the information limit of ptychography can surpass the diffraction limit of $0.5\lambda/\sin(\alpha + \beta)$ by taking advantage of multiple scattering. A [001]-orientated $DyScO_3$ single crystal sample is used for the experiment. The sample thickness is determined as 25 nm using the adaptive-propagator algorithm demonstrated in Ref. [13]. Four-dimensional datasets are acquired using an electron microscope pixel array detector (EMPAD) [29] under a high voltage of 300 kV and convergence semiangle α of 25 mrad. Each diffraction pattern contains 128×128 pixels. Different camera lengths are used to get reciprocal sampling intervals of 0.055, 0.042, 0.026, and 0.021 $Å^{-1}$ (corresponding collection semiangles β: 67, 51, 32, and 26 mrad). The results of $\beta = 26$ mrad ($\sim1.0\alpha$) and 51 mrad ($\sim2.0\alpha$) are shown in Fig. 2, those of $\beta = 32$ mrad ($\sim1.3\alpha$) and 67 mrad ($\sim2.7\alpha$) are shown in Fig. S3 [28]. The position-averaged CBEDs (PACBEDs) are shown as insets in Fig. 2. For a fair comparison, diffraction patterns in the first three datasets are all zero-padded to 154 mrad to make sure the real space pixel size of the recovered phase image reaches 64 pm. Because of the limit of GPU memory, diffraction patterns with $\beta =$ 26 mrad are only padded to 132 mrad, corresponding to a real space pixel size of 75 pm. The sample is divided into 3-Å slices during reconstruction. More detailed parameters are listed in Table S2 [28]. The recovered phase images are

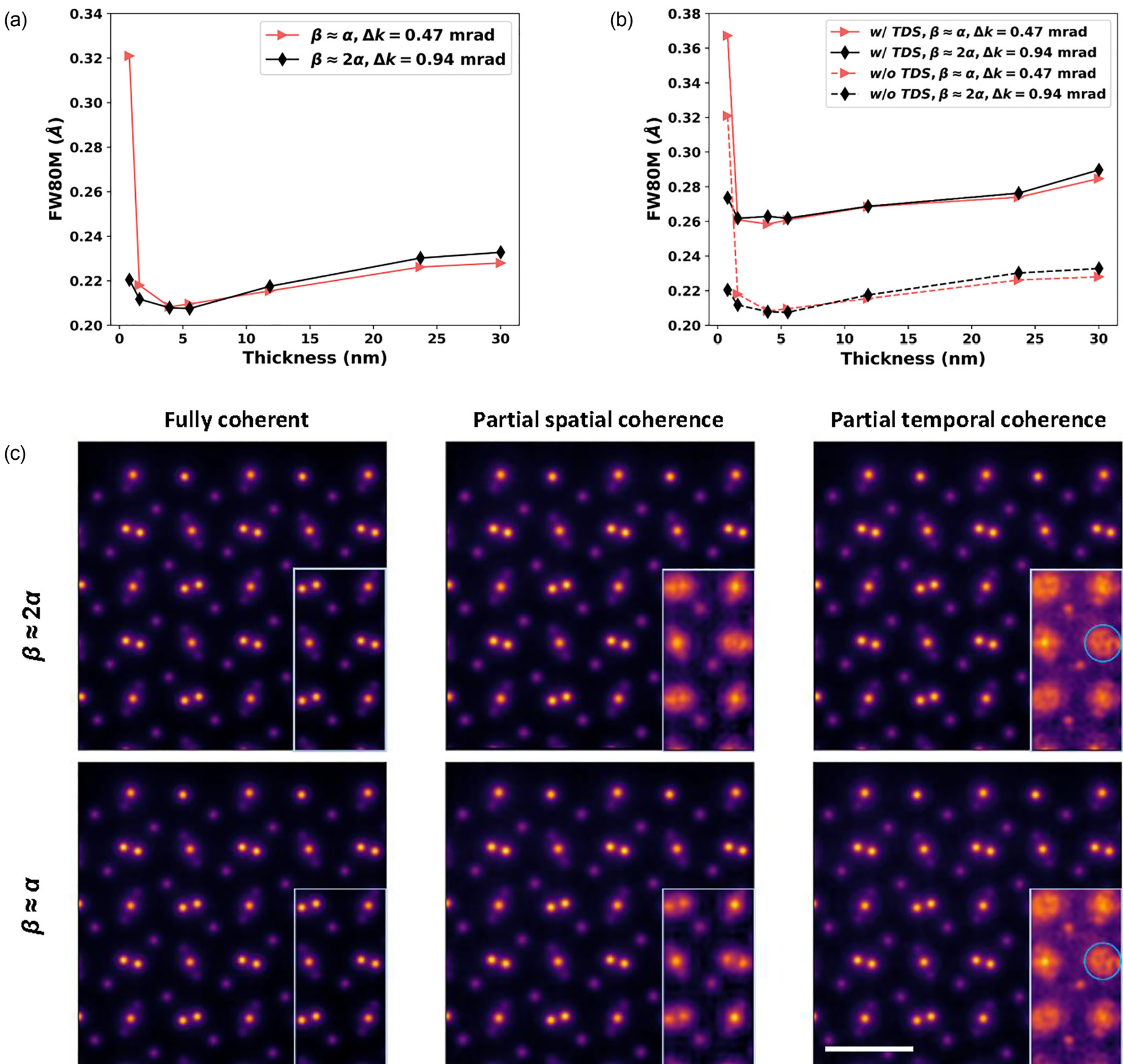

FIG. 3. Influence of thermal diffuse scattering (TDS) and partial coherence on the resolution of multislice ptychography. (a), (b) FW80M of oxygen columns in the phases recovered using datasets with different collection angles and reciprocal space sampling rates. Reconstructions with small and large collection angles are shown with red triangles and brown diamonds, respectively. (a) Noise-free datasets without considering TDS. (b) Poisson noise is added to the simulated datasets corresponding to the experimental dose value of 4×10^6 e/Å^2. (c) Total phase images summed over all the slices recovered from datasets simulated with different collection angles ($\beta \approx 2\alpha$ and $\beta \approx \alpha$) and different kinds of partial coherence. Sample thicknesses are 11.8 nm. The insets are results obtained using single probe state.

shown in Figs. 2(a) and 2(b). From the power spectra shown in Figs. 2(c) and 2(d), we can see that the resolution improves with smaller collection angles. For the condition of $\beta \approx 2\alpha$ [Figs. 2(a) and 2(c)], the information limit reaches 18 pm, overcoming the limit of $\lambda/(\alpha + \beta)$. Further refining the sampling in reciprocal space promotes the information limit to 15 pm [Figs. 2(b) and 2(d)], which corresponds to $0.44\lambda/(\alpha + \beta)$, breaking the diffraction limit in the strictest sense.

The experimental results confirm the enhancement effect of multiple scattering to the ptychographic resolution. For a specific pixelated detector, decreasing Δk results in a smaller collection angle. However, as the simulation predicted, the negative effect of smaller β is compensated by multiple scattering. With an adequate electron dose, fine reciprocal sampling further makes the high-frequency information generated by multiple scattering in diffraction patterns be better

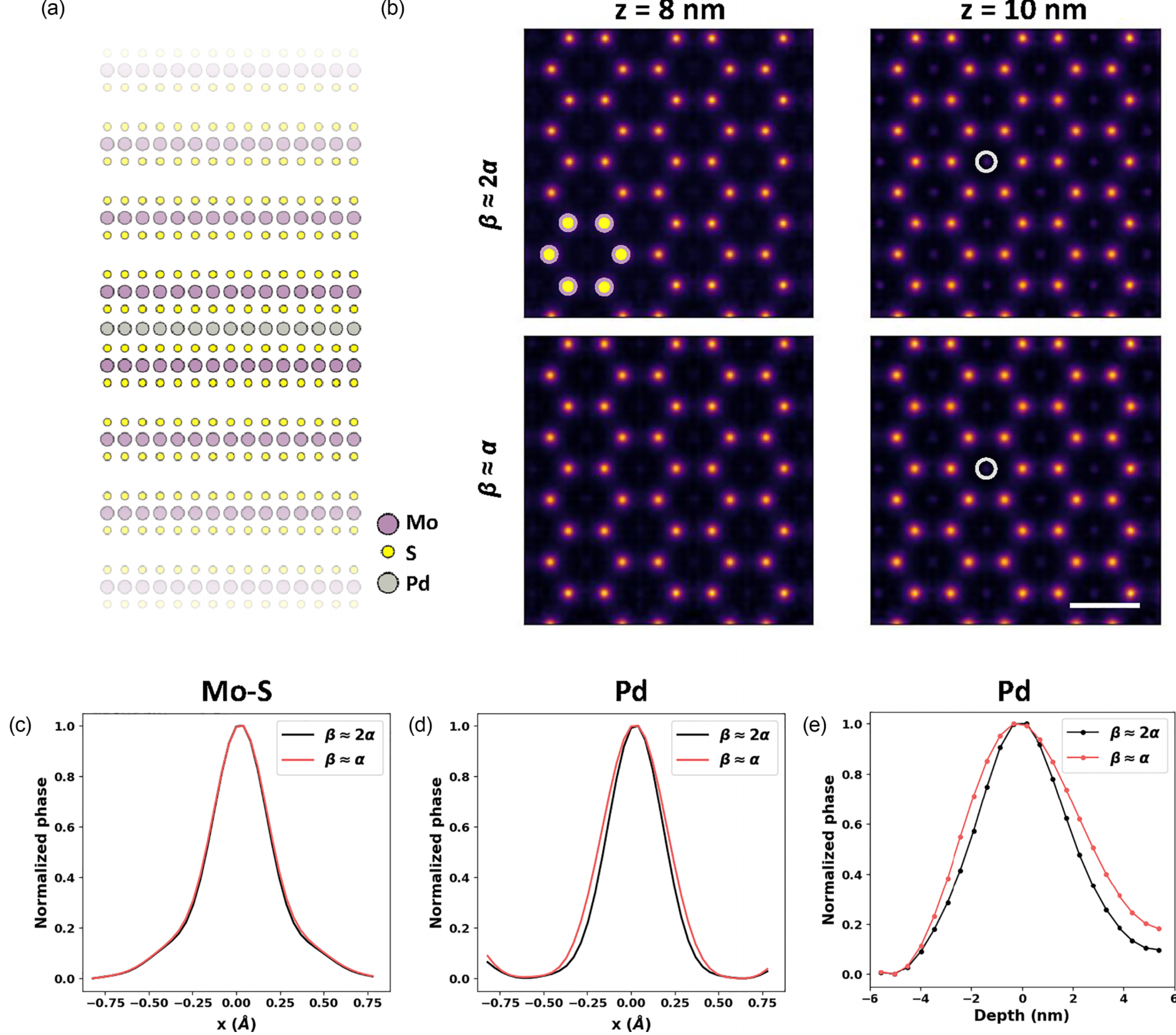

FIG. 4. Multislice reconstruction of Pd-intercalated MoS_2. (a) Cross section of the structure model used for simulation. The purple, yellow, and gray circles stand for Mo, S, and Pd atoms. (b) Phases at different depths recovered using datasets simulated with different collection angles. The white circles mark out one of the Pd atoms. Scale bar, 3 Å. (c), (d) In-plane profiles of Mo-S (c) and Pd (d) atomic columns. (e) Depth profiles of Pd atomic columns.

decoded, prompting the resolution of recovered phase images. Consequently, even under the condition of $\beta \approx \alpha$, the information limit reaches 15 pm.

To analyze the relationship between the magnitude of multiple scattering and the resolution of ptychographic phases in detail, we performed extensive multislice simulations of CBEDs and ptychographic reconstructions for samples with a series of thicknesses. The full widths at 80% of the maximum (FW80Ms) of oxygen columns were measured and used to assess the resolution of ptychographic phases (Fig. 3). FW80Ms of oxygen columns in the ptychographic phase images are shown with triangles and diamonds in Fig. 3 for small and large collection angles, respectively. Reconstruction results in Fig. 3(a) are based on noise-free datasets without considering the thermal diffuse scattering. Results in Fig. 3(b) are based on datasets under the same electron dose value with the experiment (4×10^6 e/Å^2). The solid curves show results with TDS, while the dashed curves are results without considering TDS. As the number of pixels of the detector is fixed in experiments, the dataset with a large collection angle means a low sampling rate (Δk) in the diffraction patterns. When reconstructing using only the bright-field disks ($\beta \approx \alpha$), the resolution of ptychographic phases is observed to improve for samples that are thinner than ~6 nm as the sample thickness increases. It indicates that more high-frequency information is encoded in the BF disk by multiple scattering. Consistent with the results shown in Fig. 1, as the sample thickness increases, the difference in the resolution obtained from large and small collection angles decreases, indicating that multiple scattering renders the BF disk high-frequency information.

As the sample becomes thicker than ∼6 nm, resolution in ptychographic phases decreases with sample thickness. One of the possible reasons is that strong multiple scattering generates fine features in CBEDs, which vary more rapidly than the sampling rate in reciprocal space (the detector plane). In this condition, the diffraction intensity will be undersampled and the high-frequency information cannot be well decoded by ptychography. Therefore, we conclude that instead of using a larger collection angle, reducing Δk is more useful for achieving higher resolution for thick samples that generate strong multiple scattering. Using detectors with more pixels and a sufficient dynamic range will also help.

To summarize, the limiting factor for ptychographic resolution varies with sample thickness. For samples thinner than ∼6 nm, ptychographic resolution is limited by the collection angle; a larger collection angle results in higher resolution. For thicker samples, ptychographic resolution is limited by the sampling rate in diffraction patterns; fine sampling is required to take full use of the information encoded in the diffraction patterns. Recently, Gilgenbach *et al.* also suggest that relatively large Ronchigram magnification (i.e., fine sampling in diffraction patterns) leads to better convergence of multislice electron ptychography [30].

Electron dose is another important factor limiting the resolution of ptychography [11,31–34]. As shown in Fig. 3(b), the ptychographic resolution using a large collection angle is more easily degraded by Poisson noise, especially for a thin sample. This is as expected because a high-angle scattering signal is much weaker than the signal in the bright-field disk and thin samples generally scatter fewer electrons to a high angle than thick samples. It is worthwhile to have a more detailed discussion about balancing sampling rate in diffraction space and collection angle under different magnitudes of noise and multiple scattering.

High-frequency information in diffraction intensity is easy to be degraded by partial coherence, such as partial spatial coherence caused by finite source size and partial temporal coherence related to energy spread and chromatic aberrations. Here, simulations with partial coherence are conducted with abTEM [35]. $DyScO_3$ 11.8 nm thick in the [001] direction is used to simulate the 4D datasets. Simulation parameters are kept the same as in previous simulations. The effective source size is 1.6 Å. The energy spread and chromatic aberration is 0.7 eV and 2 mm, respectively. Figure 3(c) shows the reconstruction results. The mixed-states method has been proposed to solve the problem of partial coherence in ptychography [36]. During the reconstruction of simulated datasets, four probe states are incorporated. The phases recovered without using the mixed-states method are also shown for comparison. Overall, both spatial and temporal incoherence would blur the recovered phase images even using the mixed-states method. The mixed-states method plays a crucial role to alleviate the effect of partial coherence in the reconstruction of a thick sample. In the presence of partial coherence, lateral resolution achieved by only the BF disk ($\beta \approx \alpha$) still maintains the same as the resolution obtained with a large collection angle ($\beta \approx 2\alpha$), indicating that the enhancement of the resolution by multiple scattering is robust to partial coherence.

At last, we conduct simulations to extend the discussion to depth resolution. A single layer of Pd is embedded in the 20-nm-thick MoS_2 [Fig. 4(a)]. All the simulation parameters are kept the same as in previous simulations (listed in Table S3 [28]). Poisson noise is added to the simulated datasets corresponding to a dose of 4×10^6 e/Å^2. Figure 4(b) shows the depth sections of the object phase recovered under large ($\beta \approx 2\alpha$) and small collection angles ($\beta \approx \alpha$). Movie S1 of the Supplemental Material shows all the slices [28]. The Pd layer is visible in both cases, but the phase is weaker when using a small collection angle. The in-plane profiles of Mo-S and Pd columns are used to assess the lateral resolution. The depth profiles of Pd columns are used to assess the depth resolution. As shown in Fig. 4(c), lateral resolutions of Mo-S columns obtained from large ($\beta \approx 2\alpha$) and small collection angles ($\beta \approx \alpha$) are almost the same. By contrast, both lateral [Fig. 4(d)] and depth resolutions [Fig. 4(e)] of Pd columns are improved by using a larger collection angle. The different behavior of Mo-S and Pd columns can be attributed to the weaker multiple scattering of the single Pd layer: there is not sufficient high-frequency information of Pd encoded in the BF disk and thus the lateral and depth resolution can be enhanced with larger collection angle.

In conclusion, we show that multislice ptychography is capable of decoding high-frequency information encoded in the bright-field disk. With the aid of multiple scattering, it is possible to achieve resolution beyond the diffraction limit, notably without relying on high-angle scattering.

This work was supported by the National Natural Science Foundation of China (Grant No. 52388201).

[1] E. Abbe, XV.-The relation of aperture and power in the microscope (continued)*, J. R. Microsc. Soc. **3**, 790 (1883).

[2] Lord Rayleigh F. R. S., Investigations in optics, with special reference to the spectroscope, Philos. Mag. (1798-1977) **8**, 261 (1879).

[3] C. M. Sparrow, On spectroscopic resolving power, Astrophys. J. **44**, 76 (1916).

[4] A. J. den Dekker and A. van den Bos, Resolution: A survey, J. Opt. Soc. Am. A **14**, 547 (1997).

[5] O. Scherzer, The theoretical resolution limit of the electron microscope, J. Appl. Phys. **20**, 20 (1949).

[6] Y. Peng, M. P. Oxley, A. R. Lupini, M. F. Chisholm, and S. J. Pennycook, Spatial resolution and information transfer in scanning transmission electron microscopy, Microsc. Microanal. **14**, 36 (2008).

[7] V. Intaraprasonk, H. L. Xin, and D. A. Muller, Analytic derivation of optimal imaging conditions for incoherent imaging in aberration-corrected electron microscopes, Ultramicroscopy **108**, 1454 (2008).

[8] E. G. Bosch and I. Lazic, Analysis of HR-STEM theory for thin specimen, Ultramicroscopy **156**, 59 (2015).

[9] M. J. Humphry, B. Kraus, A. C. Hurst, A. M. Maiden, and J. M. Rodenburg, Ptychographic electron microscopy using

high-angle dark-field scattering for sub-nanometre resolution imaging, Nat. Commun. **3**, 730 (2012).
[10] Y. Jiang, Z. Chen, Y. Han, P. Deb, H. Gao, S. Xie, P. Purohit, M. W. Tate, J. Park, S. M. Gruner, V. Elser, and D. A. Muller, Electron ptychography of 2D materials to deep sub-angstrom resolution, Nature (London) **559**, 343 (2018).
[11] Z. Chen, M. Odstrcil, Y. Jiang, Y. Han, M. H. Chiu, L. J. Li, and D. A. Muller, Mixed-state electron ptychography enables sub-angstrom resolution imaging with picometer precision at low dose, Nat. Commun. **11**, 2994 (2020).
[12] Z. Chen, Y. Jiang, Y. T. Shao, M. E. Holtz, M. Odstrcil, M. Guizar-Sicairos, I. Hanke, S. Ganschow, D. G. Schlom, and D. A. Muller, Electron ptychography achieves atomic-resolution limits set by lattice vibrations, Science **372**, 826 (2021).
[13] H. Sha, J. Cui, and R. Yu, Deep sub-angstrom resolution imaging by electron ptychography with misorientation correction, Sci. Adv. **8**, eabn2275 (2022).
[14] C. Liu, J. Cui, Z. Cheng, B. Zhang, S. Zhang, J. Ding, R. Yu, and E. Ma, Direct observation of oxygen atoms taking tetrahedral interstitial sites in medium-entropy body-centered-cubic solutions, Adv. Mater. **35**, e2209941 (2023).
[15] C. S. Allen, M. Danaie, J. H. Warner, D. J. Batey, and A. I. Kirkland, Super-resolution electron ptychography of low dimensional materials at 30 keV: Beyond the detector limit, Appl. Phys. Lett. **123**, 023101 (2023).
[16] P. M. Pelz, S. M. Griffin, S. Stonemeyer, D. Popple, H. DeVyldere, P. Ercius, A. Zettl, M. C. Scott, and C. Ophus, Solving complex nanostructures with ptychographic atomic electron tomography, Nat. Commun. **14**, 7906 (2023).
[17] C. W. McCutchen, Superresolution in microscopy and the Abbe resolution limit, J. Opt. Soc. Am. **57**, 1190 (1967).
[18] I. M. Vellekoop, A. Lagendijk, and A. P. Mosk, Exploiting disorder for perfect focusing, Nat. Photonics **4**, 320 (2010).
[19] Y. Choi, T. D. Yang, C. Fang-Yen, P. Kang, K. J. Lee, R. R. Dasari, M. S. Feld, and W. Choi, Overcoming the diffraction limit using multiple light scattering in a highly disordered medium, Phys. Rev. Lett. **107**, 023902 (2011).
[20] R. W. Gerchberg, Super-resolution through Error Energy Reduction, Opt. Acta **21**, 709 (2010).
[21] A. M. Maiden, M. J. Humphry, F. Zhang, and J. M. Rodenburg, Superresolution imaging via ptychography, J. Opt. Soc. Am. A **28**, 604 (2011).
[22] R. Vincent and P. A. Midgley, Double conical beam-rocking system for measurement of integrated electron diffraction intensities, Ultramicroscopy **53**, 271 (1994).
[23] P. A. Midgley and A. S. Eggeman, Precession electron diffraction - a topical review, IUCrJ **2**, 126 (2015).
[24] A. M. Maiden, M. J. Humphry, and J. M. Rodenburg, Ptychographic transmission microscopy in three dimensions using a multi-slice approach, J. Opt. Soc. Am. A **29**, 1606 (2012).
[25] A. Suzuki, S. Furutaku, K. Shimomura, K. Yamauchi, Y. Kohmura, T. Ishikawa, and Y. Takahashi, High-resolution multislice x-ray ptychography of extended thick objects, Phys. Rev. Lett. **112**, 053903 (2014).
[26] J. M. Cowley and A. F. Moodie, The scattering of electrons by atoms and crystals. I. A new theoretical approach, Acta Crystallogr. **10**, 609 (1957).
[27] P. Goodman and A. F. Moodie, Numerical evaluations of N-beam wave functions in electron scattering by the multi-slice method, Acta Crystallogr., Sect. A **30**, 280 (1974).
[28] See Supplemental Material at http://link.aps.org/supplemental/10.1103/PhysRevB.110.L060104 for extension of Figs. 1 and 2, Fourier ring correlation analysis, and detailed simulation and reconstruction parameters.
[29] M. W. Tate, P. Purohit, D. Chamberlain, K. X. Nguyen, R. Hovden, C. S. Chang, P. Deb, E. Turgut, J. T. Heron, D. G. Schlom, D. C. Ralph, G. D. Fuchs, K. S. Shanks, H. T. Philipp, D. A. Muller, and S. M. Gruner, High dynamic range pixel array detector for scanning transmission electron microscopy, Microsc. Microanal. **22**, 237 (2016).
[30] C. Gilgenbach, X. Chen, and J. M. LeBeau, A methodology for robust multislice ptychography, Microsc. Microanal. ozae055 (2024).
[31] T. Seki, Y. Ikuhara, and N. Shibata, Theoretical framework of statistical noise in scanning transmission electron microscopy, Ultramicroscopy **193**, 118 (2018).
[32] J. Song, C. S. Allen, S. Gao, C. Huang, H. Sawada, X. Pan, J. Warner, P. Wang, and A. I. Kirkland, Atomic resolution defocused electron ptychography at low dose with a fast, direct electron detector, Sci. Rep. **9**, 3919 (2019).
[33] T. J. Pennycook, G. T. Martinez, P. D. Nellist, and J. C. Meyer, High dose efficiency atomic resolution imaging via electron ptychography, Ultramicroscopy **196**, 131 (2019).
[34] C. M. O'Leary, G. T. Martinez, E. Liberti, M. J. Humphry, A. I. Kirkland, and P. D. Nellist, Contrast transfer and noise considerations in focused-probe electron ptychography, Ultramicroscopy **221**, 113189 (2021).
[35] J. Madsen and T. Susi, abTEM: A fast and flexible python-based multislice simulation package for transmission electron microscopy, Microsc. Microanal. **29**, 680 (2023).
[36] P. Thibault and A. Menzel, Reconstructing state mixtures from diffraction measurements, Nature (London) **494**, 68 (2013).